ADDITIVE MANUFACTURING OF LATTICE STRUCTURES FOR CATALYST APPLICATIONS

Nahal Ghanadi
Oregon State University
Corvallis, OR

Kwangtae Son
Oregon State University
Corvallis, OR

Brian K. Paul
Oregon State University
Corvallis, OR

Somayeh Pasebani
Oregon State University
Corvallis, OR

ABSTRACT

The design and fabrication of Inconel 718 open-pore lattice structures via Laser Powder Bed Fusion (LPBF) has been investigated in this research, focusing on applications such as catalyst supports in jet fuel production. The study explores the impact of laser power and scanning speed on the geometrical resolution of these structures aiming to achieve high porosity (porosity > 60%) and specific pore sizes ranging from 500-1000 μm, intending to serve as catalyst supports, replacing conventionally manufactured foams to reduce costs. Results demonstrate the significant influence of processing parameters on the geometrical aspects of printed lattice structures, with laser power having a more pronounced effect on geometrical accuracy than scanning speed. Additionally, the mechanical properties of the printed lattice structures showed a correlation with the lattice strut sizes, as lattices with less porosity and thicker struts resulted in higher maximum shear stress.

Keywords: Additive manufacturing; Laser powder bed fusion; Lattice structure; Surface morphology; Microstructural characterization

1. INTRODUCTION

The rapid increase in greenhouse gas emissions, particularly nitrous oxide, carbon dioxide, and methane from fossil fuel combustion and anthropogenic activities, threatens global ecological balance [1]. This rising environmental concern has heightened the need for renewable fuels to reduce reliance on exhaustible energy sources like coal, oil, and natural gas [2]. In aviation, where petroleum-based fuels predominate, adopting alternatives is crucial for reducing carbon emissions [3]. Alternative fuels are advantageous for their reduced emissions, renewable properties, and decreased dependence on fossil fuels. They must possess high energy density, typically found in C8-16 liquid iso-hydrocarbons, and have low freezing points, efficient cold flow properties, and thermal stability to ensure compatibility with existing engines [4].

Biomass and petroleum differ in chemical composition, necessitating distinct fuel production approaches [5]. While deoxygenated petroleum hydrocarbons require high-temperature gas-phase processing, the oxygen-rich biomass calls for lower-temperature treatments to eliminate oxygen and modify molecular structures. Biomass conversion to jet fuel includes dehydration, hydrogenation, and decarboxylation, followed by catalytic reactions to enhance molecular weight, and remove oxygen. Alumina-based catalysts are essential for converting alcohols to hydrocarbons in bio-jet fuel synthesis [6,7]. The catalytic oligomerization process efficiently transforms dehydrated ethylene to linear α-olefins, crucial for renewable jet fuels. Additionally, the γ-alumina catalytic conversion of n-butanol to 1-butene with high bio-butene selectivity highlights the adaptability of alumina catalysts in renewable fuel production [8].

For selecting materials to be used as catalytic scaffolds in jet fuel lines, commercial superalloys like Inconel 718 have been popular due to their excellent corrosion resistance and mechanical properties at high temperatures, up to 600 °C [9]. Performance enhancements of these catalytic scaffolds can be achieved through coatings of various surfactants, including SiO_2 [10], silicosteel [11], chromium plating [12], or TiO_2 [13], to increase the scaffold porosity. However, economic challenges have restricted the commercialization of high-porosity structures due to the costs associated with traditional open-cell fabrication methods [14]. Additive manufacturing (AM) offers a cost-effective solution, particularly for producing highly porous structures [15]. LPBF is suitable for lattice fabrication among other AM methods due to its high precision allowing complex lattice structures to be built with excellent geometric accuracy

and mechanical integrity resulting in cost savings compared to conventional methods [16,17].

Among various techniques for creating highly porous structures with LPBF, lattice structure printing using 3D CAD modeling has been widely adopted [18]. Different lattice structures have been tested to fabricate high-porosity structures, aiming to improve performance in target applications while ensuring good porosity, mechanical properties, specific surface area, and other essential parameters. Among the various lattice designs available, the dode-medium lattice has shown significant potential for maximizing porosity in high-porous structures manufactured via LPBF [19]. For a favorable performance of the Inconel 718 catalytic scaffold fabricated by LPBF, a larger surface area is required [20]. In the Dode-medium lattice structure, the surface area is directly related to the strut size, pore size, and overall porosity. Thicker strut sizes create more surface area per unit volume. Similarly, smaller pore sizes increase the surface area since the lattice structure becomes denser, and more struts are required to form these smaller pores. However, higher porosity generally means fewer solid struts and larger pores, reducing the overall surface area. Thus, the surface area increases with thicker struts and smaller pores, while higher porosity reduces it by minimizing the amount of solid material available for surface exposure.

In the present study, our primary objective is to develop a process strategy to achieve the desired geometrical requirements i.e, pore size, strut size and porosity, for LPBF-printed dode-medium lattice Inconel 718 coupons. The effects of laser parameter control and its resulting heat input is investigated using microstructure characterization to determine the relationship between the heat input and geometrical parameters including porosity, pore size, and strut size. Particularly, Volumetric Energy Density (VED) which is calculated by considering factors such as laser power, scanning speed, layer thickness, and spot size, is used in this study as an indicator of heat input, demonstrating the amount of energy delivered to a specific volume of material.

In addition to that, mechanical properties of those printed lattice structures were evaluated using a shear test [21].

This study contributes to advancing the fabrication of metal lattice structures, impacting on the production industry and beyond, encouraging more investigation and progress in this field.

2. MATERIALS AND METHODS

The powder feedstock was gas-atomized Inconel 718 supplied from Carpenter additive (Pennsylvania, USA) with mostly spherical particle shape (Figure 1a) and chemical composition as listed in table 1. A Malvern Panalytical Mastersizer 3000 particle size analyzer (Malvern, United Kingdom) was employed to measure the powder size. The D10, D50, and D90 of the powder particle are 15 µm, 26.5 µm, and 44.9 µm, respectively. The measured powder particles size distribution is presented in Figure 1b.

Table 1. The chemical compositions of the Inconel 718 powder (wt%).

Element	Ni	Cr	Fe	Nb+Ta	Mo	Co	Ti	C	N	O	Al	Si
wt.%	54.22	18.5	17.46	4.86	3.09	0.2	1.03	0.04	0.01	0.02	0.52	0.05

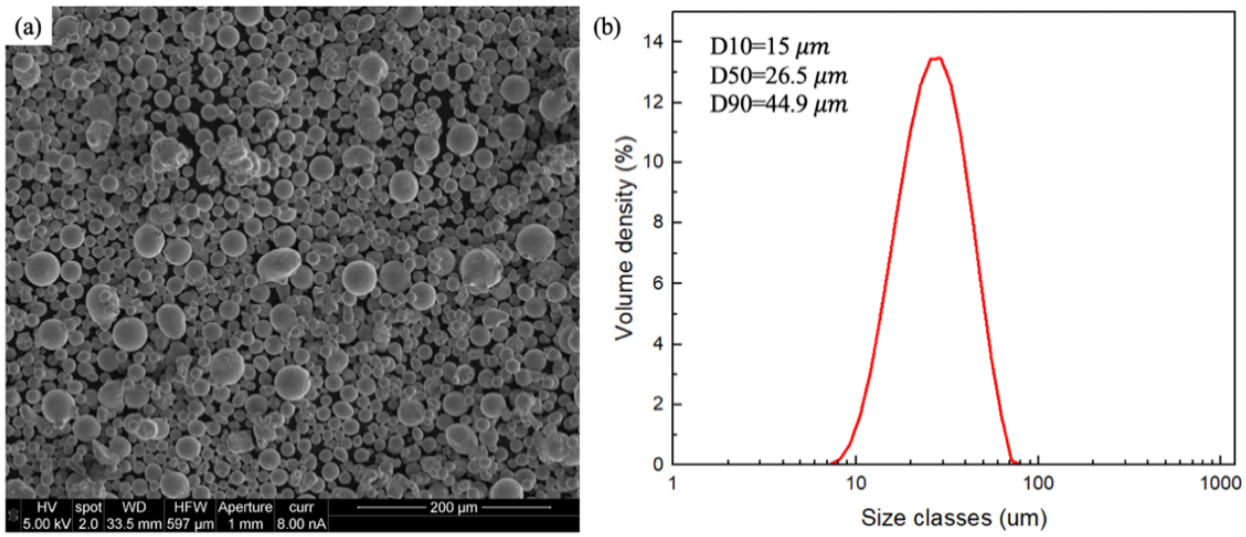

Figure 1. (a) SEM image of powder morphology and (b) powder particle size distribution.

The modeling of the dode-medium lattice structure was conducted using the Ntopology software (New York, USA) [22], provided by Dr. Hazeli's research group at the University of Arizona [23]. The dode-medium lattice structure consists of a unit cell size of 2 mm, pore size of 1.13 mm and strut thickness of 0.26 mm with all the struts oriented at 45◦ with respect to the building direction resulting in the target 80% porosity in the design.

A 2oneLab LPBF 3D printer (Darmstadt, Germany) equipped with a continuous wave fiber laser of Yb:YAG with a 1070 nm infrared laser (IR) was utilized to fabricate high-porous dode-medium lattice structure.

Dode-medium lattice structure-samples with dimensions of 7 × 7 × 7 mm were fabricated with the layer thickness, hatch spacing, and the laser spot size of 25 µm, 40 µm and 40 µm respectively. Laser powers of 50 W, and 100 W were selected to examine the effect of laser power on the characteristics of the lattice structure. The laser scanning speed was ranging from 200 – 1200 mm/s. Commercially-pure nitrogen was continuously supplied into the LPBF chamber to avoid unfavorable oxide formation during the LPBF printing. The oxygen level in the sealed build chamber was kept (<0.08 vol%) throughout the printing sequence.

An FEI Quanta 600 scanning electron microscope (SEM) were utilized for characterizing the lattice structures and the density of the lattice structures was measured using a four-digit resolution Ohaus Archimedes density measurement (New Jersey, USA). Other geometrical characteristics of the lattices such as, strut size, and pore size were quantified by averaging measurements from five cross-sectional images per each lattice structure, using ImageJ software for analysis. The closeness of the geometrical parameters of the printed parts to the solid model from the CAD file was also evaluated to derive optimal parameters for the dode-medium lattice LPBF printing.

In addition to the geometrical characteristics of the printed lattices, their mechanical property is also one other important factor to assess their functionality as the chemical catalyst scaffold. For this purpose, cylindrical lattice structures with dimensions of ϕ 5 mm × 10 mm were fabricated using the same processing parameters mentioned above, to investigate the mechanical properties of the printed lattice structure using a universal tester to investigate the effect of geometrical aspects of the lattice structure on its mechanical performance. A shear test was performed to obtain mechanical strength and ductility of those lattice samples at room temperature at a strain rate of 2 mm/mm to investigate the effect of geometrical aspects of the lattice structure on its mechanical performance.

3. RESULTS AND DISCUSSION

The surfaces morphologies of lattices fabricated using different processing parameters, specifically varying laser power (W) and scanning speed (mm/s) is illustrated in Figure 2. The Figure shows that reducing laser power or increasing the scanning speed significantly affects the geometry of the fabricated structures. Specifically, the resulting lattices exhibit larger pore sizes and progressively thinner struts, which potentially leads to higher porosity. These trends can be attributed to reduced melting caused by lower energy input under these conditions [24,25]. When the laser power is reduced or the scanning speed is increased, insufficient energy will be delivered to the powder bed, resulting in incomplete material fusion and consolidation. This leads to larger pore spaces, thinner struts, or even partial disconnection between struts. Additionally, the surface roughness of the lattices tends to increase by lowering the energy input as observed in the SEM images [26,27]. This is due to inadequate energy input preventing the proper fusion of powder particles, resulting in a rougher surface texture as un-melted particles adhere to the lattice structure.

In contrast, increasing the laser power or decreasing the scanning speed (i.e., high energy input), results in lattice structures with higher density, smaller pore sizes and thicker struts. This phenomenon can be understood through the dynamics of laser-material interaction occurring during LPBF fabrication. At higher laser powers, more energy is delivered to the powder bed, promoting wider and deeper melt pool formation and a subsequent faster cooling [28,29].

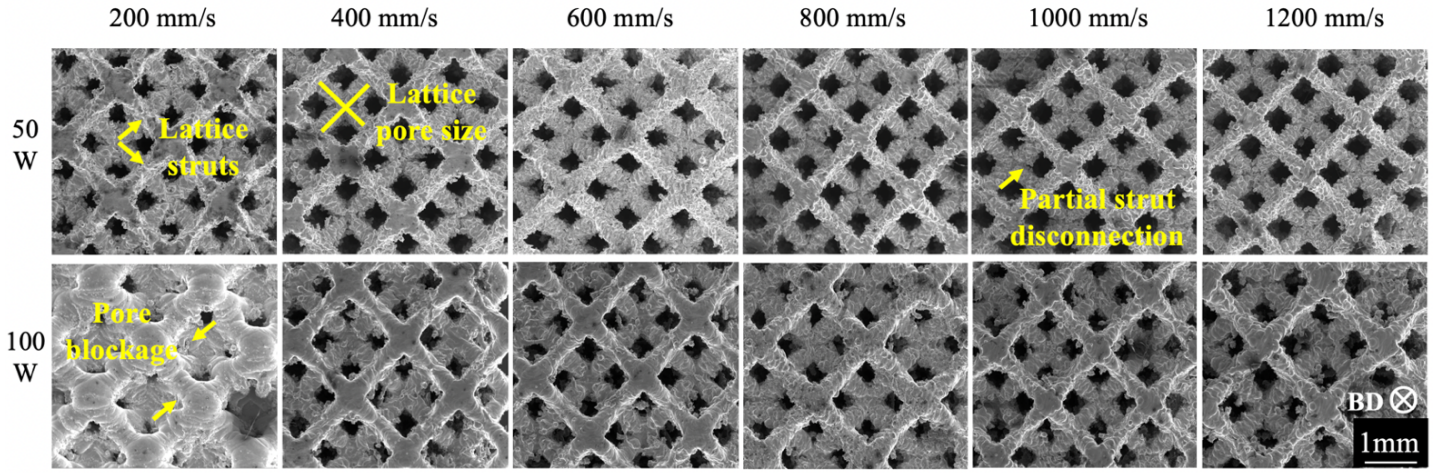

Figure 2. SEM images of the top surface morphologies of the Inconel 718 lattices fabricated with different processing parameters.

Therefore, a general conclusion can be made: a denser lattice structure is fabricated by applying higher energy input through increased laser power or reduced scanning speed.

Additionally, the prolonged laser-powder interaction due to slower scanning speeds allows for more extensive material melting, leading to a denser packing of particles. This, in turn, creates smaller pores than originally intended in the CAD design, or in some cases, causes pore blockage, as observed in lattices fabricated with power 100 W and speed 200 mm/s (Figure 2).

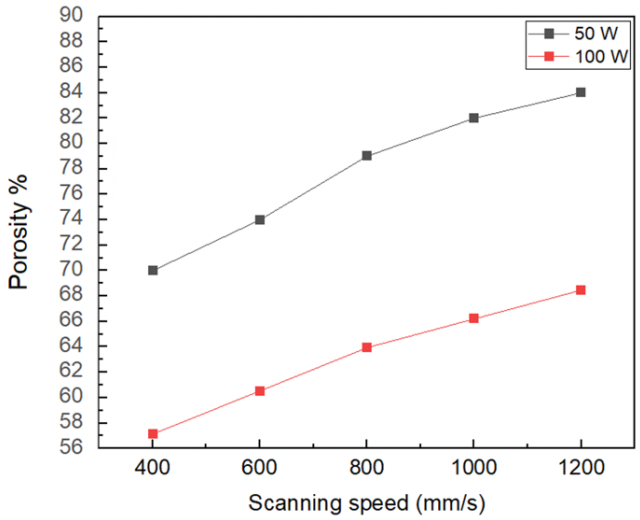

Figure 3. Variation of the porosity of the lattices as a function of laser power (W) and scanning speed (mm/s).

To visualize this effect, Figure 3 displays the measured porosity values with the Archimedes method for those lattices fabricated under laser power settings of 50 W and 100 W. In general, the porosity level tends to increase by lowering the scanning speed at the two laser powers, showing the minimum of 48 % and the maximum of 84 %. As predicted from the observation of Figure 2, the porosity values at 100 W exhibit smaller magnitudes compared to those at 50 W due to the thicker struts and excessive consolidation around the struts at 100 W.

Despite the intended porosity of 80% in the dode-medium lattice, the structures fabricated using low heat input parameters i.e., 50 W laser power and 1000-1200 mm/s scanning speed achieved porosity of > 80% which is higher than the intended design. While increased porosity is typically advantageous for lattice structures with providing lighter weight and enhanced catalytic performance [30], this higher porosity level sometimes causes unexpected consequences. Specifically, in lower energy input conditions of higher porosities, the lower heat input led to incomplete melting, resulting in thinner struts than originally designed or even disconnected struts in the lattice. While higher porosity can enhance features like light weighting and material permeability, a balance should exist between porosity control and the structural integrity of printed part.

Therefore, the optimal printing parameter for this lattice structure requires more characterization other than the porosity. The average strut sizes of the LPBF-printed lattice structures at different laser parameters are shown in Figure 4.

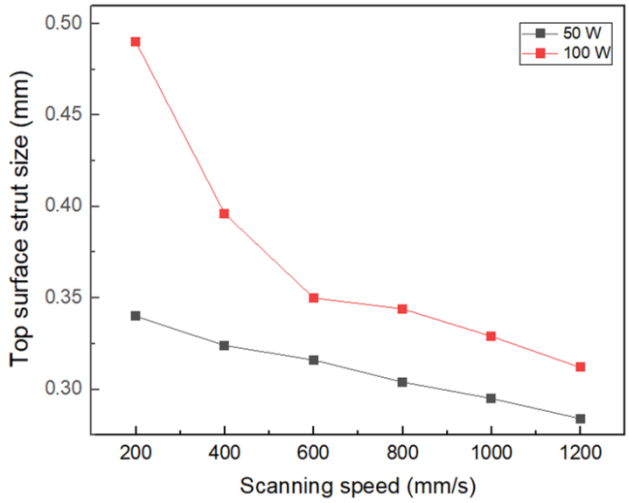

Figure 4. Variation of the top surface strut size of the lattices as a function of laser power (W) and scanning speed (mm/s).

Consistent with the previous discussion on Figure 2, as scanning speed increases from 200 to 1200 mm/s, strut thickness of lattice structures gradually decrease in both 50 W and 100 W. In the 100 W condition, the strut size reduction by lowering scanning speed is more significant at the slow scan speed regime of 200 – 600 mm/s. Beyond that regime, the slope for the strut size reduction with respect to increasing scanning speed at 100 W becomes comparable with that of the 50 W condition.

SEM images of the side surface of the lattices highlight distinct differences between the top and side surfaces of the fabricated lattice structures. As can be seen in Figure 5, side surfaces exhibit smaller pores and thicker struts with more pronounced powder attachment compared to the top surface.

During the printing process, molten material is affected by gravitational forces, which cause it to flow downward and settle more readily into the existing structure. This gravitational settling encourages the material to fill gaps, particularly along the side surfaces that are already partially enclosed by previous layers [31]. Meanwhile, un-melted powder particles tend to accumulate and adhere more strongly to the side surfaces, further reinforcing these regions and reducing the likelihood of the intended pore structure generation. In addition to the influence of gravity on the pore characteristics of the side surface, these variations can be attributed to several other factors. The surface morphology of lattice structures, particularly on the side surface, is heavily affected by the "staircase effect" [32,33]. This phenomenon results from the geometrical steps inherent between consecutive layers during the printing process, leading to irregular surface morphology transitions along the struts.

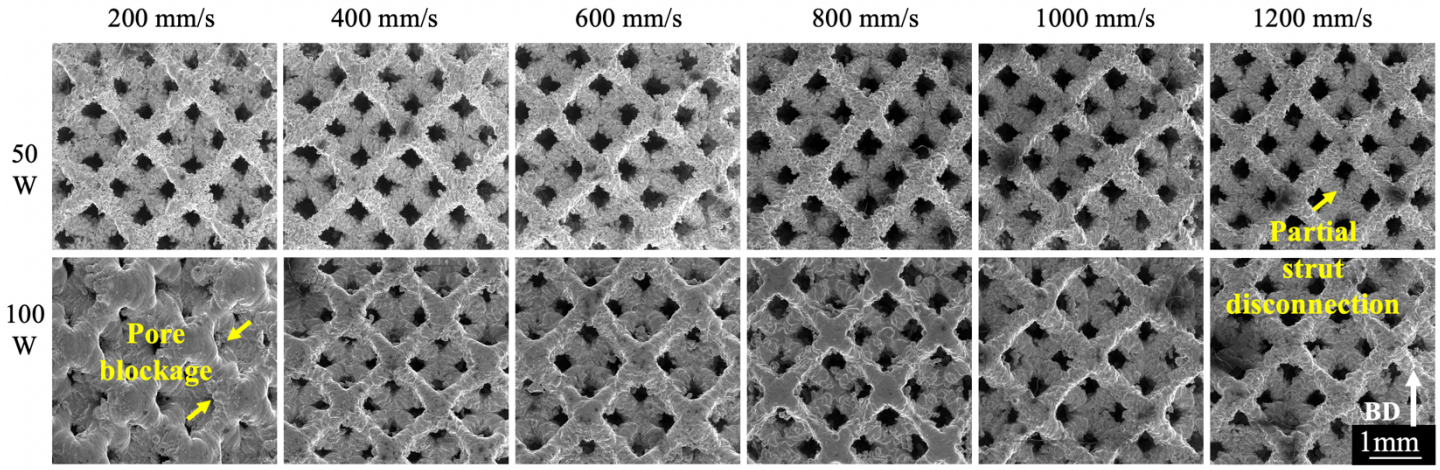

Figure 5. SEM images of the side surface morphologies of the Inconel 718 lattices fabricated with different processing parameters.

Furthermore, the side surfaces have increased exposure to the laser beam during layer-by-layer fabrication, resulting in higher localized temperatures [34,35]. Heat accumulation within the molten pool, due to the low thermal conductivity of the powder bed, intensifies this effect. Additionally, the high temperatures and recoil pressure generate capillary forces within the melt pool, causing the molten material to flow into the adjacent powder.

With lower energy input resulting from the reduced laser power and faster scanning speed material melting and remelting of the previous layers is minimized leading to reduction of capillary forces and recoil pressure [36,37]. Consequently, there is fewer excessive material to be drawn into the gaps between powder particles, thus reducing the flow of molten material into the surrounding powder and the accumulation of powder on the side surfaces. In other words, the pore closure is less evident in the lower energy input conditions when it is compared with the higher energy input conditions.

Figure 6 shows the difference in pore sizes between the two surfaces. In all LPBF conditions, the side surface exhibits smaller pore sizes than the top surface due to increased powder consolidation around the build area during the LPBF process. One consistent observation between the top and side views is that pore size increases at higher scanning speeds while maintaining the same laser power. For lattice structures fabricated at 50 W, increasing the scanning speed from 200 mm/s to 1200 mm/s resulted in a 20% increase in pore size on the top surface and a 29% increase on the side surface. Similarly, for lattice structures fabricated at 100 W laser power, the pore size increased by 18% on the top surface and 29% on the side surface when the scanning speed was increased.

This more pronounced increase in pore size on the side surface compared to the top surface highlights that the side surfaces of lattice structures are subject to different thermal and fluid dynamic conditions than the top surface when subjected to similar changes in processing parameters as the low heat input minimizes the melting and remelting of the previously fabricated layer and introduces lower levels of heat accumulation.

Moreover, it can be observed that the size difference between the top and side pores decreases with decreasing the heat input. This suggests that with lower heat input the effect of recoil pressure and capillary forces is minimized on the side surfaces resulting in more consistency in pore size throughout the structure.

Consistent with the observed increase of pore size, the strut thickness of the side surfaces follows a similar trend as top surface as demonstrated in Figure 7.

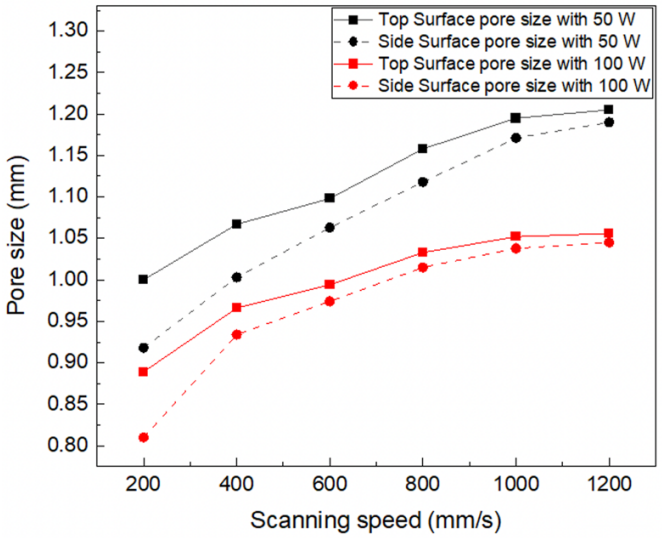

Figure 6. Variation of the top and side surface pore size of the lattices as a function of laser power (w) and scanning speed (mm/s).

Table 2 presents an overview of the various processing conditions tested, i.e., laser powers of 50 W and 100 W, along with scanning speeds ranging from 200 to 1200 mm/s. Each condition is evaluated based on parameters such as the heat input (VED), porosity and the pore sizes. Among the tested conditions, the lattice fabricated with 50 W laser power and a scanning speed of 800 mm/s exhibited the least deviation from the designed dode-medium lattice. The porosity of this lattice closely matched

the design specifications, showing the effectiveness of this specific processing parameter combination in achieving the desired structural characteristics.

While VED has been accepted as an integrated processing parameter to predict micro/macro structure of the printed part in LPBF [38], this general concept is observed to be an improper indicator in this study. For example, the lattices fabricated with 50 W laser power and 400 mm/s scanning speed, and 100 W laser power and 800 mm/s scanning speed have the same VED of 125 J/mm^3. Despite both structures having the same VED, the lattice fabricated under 50 W laser power and 400 mm/s scanning speed exhibits a higher porosity of 79%, larger pore size and thinner struts, while the lattice fabricated under 100 W laser power and 800 mm/s scanning speed has a lower porosity of 63%, smaller pores and thicker struts (Figure 8).

The differences in those geometrical properties such as porosity and structural characteristics with different laser power and scanning speed are due to different thermal dynamics, cooling rates, the distribution and dissipation of heat within the powder bed between the two cases. In particular, the melt pool dynamics including peak temperature and cooling rate are more sensitive to the variation in the laser power than the change in the scanning speed [39,40].

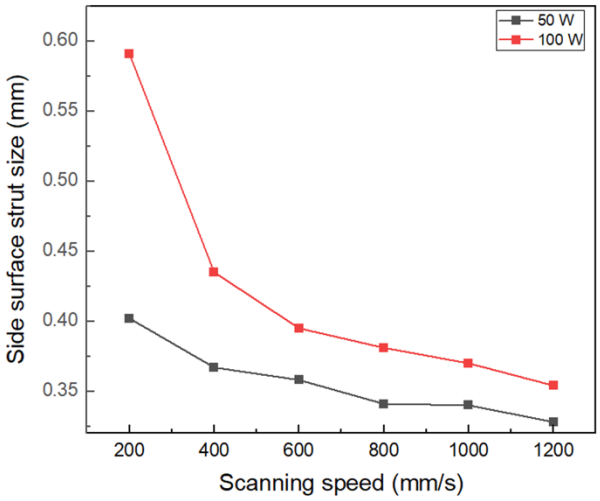

Figure 7. Variation of the side surface strut size of the lattices as a function of laser power (w) and scanning speed (mm/s).

Table 2. Characterizations of the lattices fabricated via LPBF process under various laser power and scanning speeds. (CAD-designed values: porosity = 80 % and pore size = 1.13 mm)

Power (W)	Scanning Speed (mm/s)	VED (J/mm^3)	Measured Porosity	Measured top surface pore size (mm)	Measured side surface pore size (mm)
50	200	250	63%	1±0.068	0.918±0.039
50	400	125	70%	1.067±0.058	1.003±0.052
50	600	83.3	73%	1.098±0.056	1.063±0.027
50	800	62.5	79%	1.158±0.081	1.118±0.049
50	1000	50	82%	1.195±0.193	1.171±0.018
50	1200	41	84%	1.205±0.047	1.19±0.074
100	200	500	48%	0.889±0.184	0.81±0.156
100	400	250	57%	0.966±0.155	0.934±0.022
100	600	166.7	60%	0.994±0.063	0.974±0.032
100	800	125	63%	1.033±0.186	1.015±0.127
100	1000	100	65%	1.052±0.049	1.038±00.026
100	1200	83.3	67%	1.056±0.165	1.045±0.035

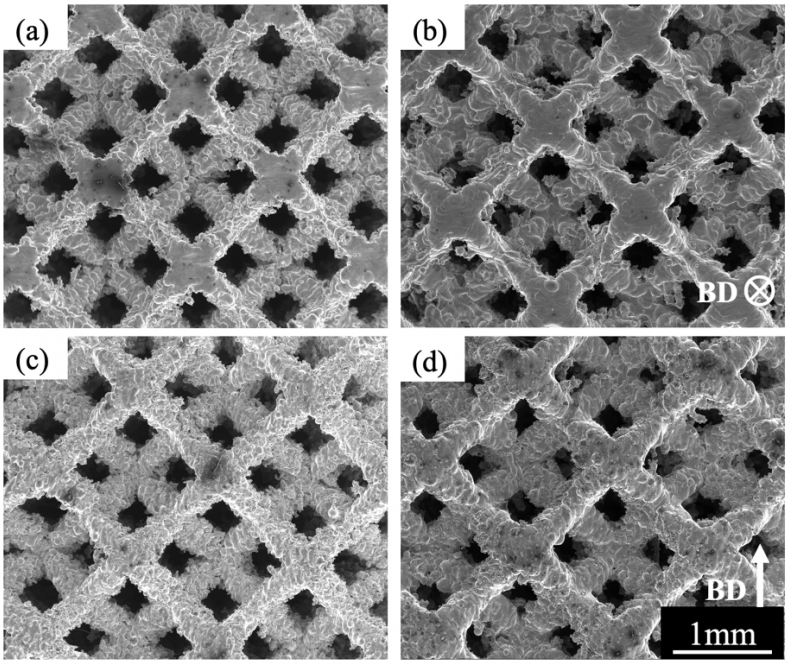

Figure 8. (a) and (c) top and side surface of lattices fabricated with VED=125 J/mm^3 and P=50 W. (b) and (d) top and side surface of lattices fabricated with VED=125 J/mm^3 and P=100 W.

In addition to geometric parameters, mechanical properties are crucial for assessing the durability of catalytic scaffolds in their application environments. The shear test results for LPBF-printed lattice structures are presented in Table 3. An investigation of lattices fabricated under varying processing parameters reveals distinct trends in ultimate shear stress across different combinations of laser power and scanning speed.

Thinner strut lattices, fabricated with lower heat input (indicated by lower laser power and faster scanning speeds), showed lower maximum shear stress values. On the other hand, thicker strut lattices, fabricated under higher heat input (i.e., high laser power and slower scanning speeds), exhibited higher maximum shear stress values.

Table 3. Summary of the maximum shear stress for each of the fabricated samples.

Power (W)	**Speed (mm/s)**	**VED (J/mm^3)**	**Maximum shear stress (Mpa)**
100	200	500	122
100	400	222	64
100	600	166	55
100	800	125	48
100	1000	100	44
100	1200	83.3	44
50	200	250	38
50	400	125	24
50	600	83	21
50	800	62.5	15
50	1000	50	14
50	1200	41	14

The decrease in shear strength with decreasing the heat input is not linear and the reduction in maximum shear strength is more pronounced between higher VEDs. Meanwhile, differences in maximum shear strength among lower VEDs are more subtle. At higher energy inputs or VEDs, a relatively more extensive heat would be supplied on the powder bed, leading to greater melting and fusion of powder particles. This results in lattices with better consolidation or reducing cavity formation within the struts, and thicker struts, all of which enhance the structural integrity of the lattice, allowing it to withstand higher shear stress until rupture. As the VED decreases, however, the melting and fusion process becomes less extensive, leading to higher overall porosity, thinner struts, and defects such as a lack of fusion. This results in structures with lower maximum shear stress.

Furthermore, within the same VED levels, lattices fabricated with higher laser power exhibited thicker struts and consequently higher maximum shear stress than their lower-power counterparts. This suggest that the VED is not an appropriate parameter to describe the geometrical aspects in the dode-medium lattice structure printed by LPBF.

4. CONCLUSION

This study explored the relationship between processing parameters and the quality of lattice structures fabricated via LPBF. Through experimentation and analysis, the effects of laser power and scanning speed variations on key structural characteristics, including porosity, pore size, and strut dimensions is investigated. Findings revealed significant correlations between processing parameters and structural integrity, with higher laser power and lower scanning speeds generally resulting in denser structures with smaller pore sizes and thicker struts. Conversely, lower laser power and higher scanning speeds led to increased porosity and thinner struts due to incomplete melting and insufficient material fusion.

Moreover, our investigation demonstrated the importance of balancing porosity control with structural integrity, as excessive porosity could compromise the mechanical performance and specific surface area of lattice structures which is detrimental to catalytic performance.

ACKNOWLEDGEMENTS

This material is based upon work supported by the U.S. Department of Energy's Office of Energy Efficiency and Renewable Energy (EERE) under the Bioenergy Technologies Office award number DE-EE0009261. The views expressed herein do not necessarily represent the views of the U.S. Department of Energy or the United States Government.

We would like to extend our gratitude to Dr. Kavan Hazeli's research group at the University of Arizona for providing the design file of the dode-medium lattice structure. Their support and resources were invaluable to our research.

REFERENCES

(1) Xu, G.; Schwarz, P.; Yang, H. Adjusting Energy Consumption Structure to Achieve China's CO2 Emissions Peak. *Renewable and Sustainable Energy Reviews* **2020**, *122*, 109737. https://doi.org/10.1016/j.rser.2020.109737.

(2) Wei, H.; Liu, W.; Chen, X.; Yang, Q.; Li, J.; Chen, H. Renewable Bio-Jet Fuel Production for Aviation: A Review. *Fuel* **2019**, *254*, 115599. https://doi.org/10.1016/j.fuel.2019.06.007.

(3) Duan, H.; Mo, J.; Fan, Y.; Wang, S. Achieving China's Energy and Climate Policy Targets in 2030 under Multiple Uncertainties. *Energy Econ* **2018**, *70*, 45–60. https://doi.org/10.1016/j.eneco.2017.12.022.

(4) Pang, S. Advances in Thermochemical Conversion of Woody Biomass to Energy, Fuels and Chemicals. *Biotechnol Adv* **2019**, *37* (4), 589–597. https://doi.org/10.1016/j.biotechadv.2018.11.004.

(5) Chisti, Y. Constraints to Commercialization of Algal Fuels. *J Biotechnol* **2013**, *167* (3), 201–214. https://doi.org/10.1016/j.jbiotec.2013.07.020.

(6) Díaz-Pérez, M. A.; Serrano-Ruiz, J. C. Catalytic Production of Jet Fuels from Biomass. *Molecules* **2020**, *25* (4), 802. https://doi.org/10.3390/molecules25040802.

(7) Son, K.; Kao, H.-M.; McNeff, P.; Yang, S.; Ghanadi, N.; Pasebani, S.; Chang, C.-H.; Paul, B. A FeCrAl-Al2O3 Composite Produced via Laser Powder Bed Fusion of a Mixed Powder for Porous Catalyst Scaffolds. *J Micro Nanomanuf* **2024**, 1–31. https://doi.org/10.1115/1.4066114.

(8) Wang, W.-C.; Tao, L. Bio-Jet Fuel Conversion Technologies. *Renewable and Sustainable Energy Reviews* **2016**, *53*, 801–822. https://doi.org/10.1016/j.rser.2015.09.016.

(9) Altin, O.; Eser, S. Pre-Oxidation of Inconel Alloys for Inhibition of Carbon Deposition from Heated Jet Fuel. *Oxidation of Metals* **2006**, *65* (1–2), 75–99. https://doi.org/10.1007/s11085-006-9002-5.

(10) Graff, M. J.; Albright, L. F. Coke Deposition from Acetylene, Butadiene and Benzene Decompositions at 500–900°C on Solid Surfaces. *Carbon N Y* **1982**, *20* (4), 319–330. https://doi.org/10.1016/0008-6223(82)90008-2.

(11) Altin, O.; Eser, S. Analysis of Solid Deposits from Thermal Stressing of a JP-8 Fuel on Different Tube Surfaces in a Flow Reactor. *Ind Eng Chem Res* **2001**, *40* (2), 596–603. https://doi.org/10.1021/ie0004491.

(12) Fujita, M.; Jomjunyong, S.; Itoh, Y.; Yokoyama, S.; Matsumoto, S. Predicting Service Life of a Bright Ni-Cr Electroplating System on Steel Subjected to the CASS Test. *Transactions of the IMF* **1997**, *75* (3), 98–100. https://doi.org/10.1080/00202967.1997.11871151.
(13) Krishan Lal Luthra; Kee Douglas William Mac. Coating Systems for Titanium Oxidation Protection. DE4112218A1, 1991.
(14) Kulshreshtha, A.; Dhakad, S. K. Preparation of Metal Foam by Different Methods: A Review. *Mater Today Proc* **2020**, *26*, 1784–1790. https://doi.org/10.1016/j.matpr.2020.02.375.
(15) Liu, H.; Gu, D.; Yang, J.; Shi, K.; Yuan, L. Laser Powder Bed Fusion of Node-Reinforced Hybrid Lattice Structure Inspired by Crystal Microstructure: Structural Feature Sensitivity and Mechanical Performance. *Materials Science and Engineering: A* **2022**, *858*, 144048. https://doi.org/10.1016/j.msea.2022.144048.
(16) Ghanadi, N.; Pasebani, S. A Review on Wire-Laser Directed Energy Deposition: Parameter Control, Process Stability, and Future Research Paths. *Journal of Manufacturing and Materials Processing* **2024**, *8* (2), 84. https://doi.org/10.3390/jmmp8020084.
(17) Ataollahi, S. A Review on Additive Manufacturing of Lattice Structures in Tissue Engineering. *Bioprinting* **2023**, *35*, e00304. https://doi.org/10.1016/j.bprint.2023.e00304.
(18) Hyer, H.; Zhou, L.; Liu, Q.; Wu, D.; Song, S.; Bai, Y.; McWilliams, B.; Cho, K.; Sohn, Y. High Strength WE43 Microlattice Structures Additively Manufactured by Laser Powder Bed Fusion. *Materialia (Oxf)* **2021**, *16*, 101067. https://doi.org/10.1016/j.mtla.2021.101067.
(19) Hazeli, K.; Babamiri, B. B.; Indeck, J.; Minor, A.; Askari, H. Microstructure-Topology Relationship Effects on the Quasi-Static and Dynamic Behavior of Additively Manufactured Lattice Structures. *Mater Des* **2019**, *176*, 107826. https://doi.org/10.1016/j.matdes.2019.107826.
(20) Bernard, P.; Stelmachowski, P.; Broś, P.; Makowski, W.; Kotarba, A. Demonstration of the Influence of Specific Surface Area on Reaction Rate in Heterogeneous Catalysis. *J Chem Educ* **2021**, *98* (3), 935–940. https://doi.org/10.1021/acs.jchemed.0c01101.
(21) Vaziri Sereshk, M. R.; Faierson, E. J. Novel Test Method to Determine Shear Properties of Lattices: Test Set-up and Data Analysis. *Compos B Eng* **2023**, *253*, 110561. https://doi.org/10.1016/j.compositesb.2023.110561.
(22) *nTop, Release 4.4.2, nTop Inc., https://ntop.com*.
(23) Hazeli, K.; June, D.; Anantwar, P.; Babamiri, B. B. Mechanical Behavior of Additively Manufactured GRCop-84 Copper Alloy Lattice Structures. *Addit Manuf* **2022**, *56*, 102928. https://doi.org/10.1016/j.addma.2022.102928.
(24) Wang, Y.; Wang, L.; Liu, D.; Miao, B.; Wu, H.; Pei, J.; Yan, W.; Yuan, G. Mechanisms of Processing Map Difference between Laser Powder Bed Fusion of Mg Solid Cubes and Lattice Structures. *Addit Manuf* **2023**, *76*, 103773. https://doi.org/10.1016/j.addma.2023.103773.
(25) Di Prima, M.; Van Belleghem, S.; Badhe, Y.; Snodderly, K.; Porter, D.; Burchi, A.; Gilmour, L. Build Parameter Influence on Strut Thickness and Mechanical Performance in Additively Manufactured Titanium Lattice Structures. *J Mech Behav Biomed Mater* **2024**, *151*, 106369. https://doi.org/10.1016/j.jmbbm.2024.106369.
(26) Pyka, G.; Kerckhofs, G.; Papantoniou, I.; Speirs, M.; Schrooten, J.; Wevers, M. Surface Roughness and Morphology Customization of Additive Manufactured Open Porous Ti6Al4V Structures. *Materials* **2013**, *6* (10), 4737–4757. https://doi.org/10.3390/ma6104737.
(27) Boschetto, A.; Bottini, L.; Ghanadi, N. Areal Analysis Investigation of Selective Laser Melting Parts. *Journal of Manufacturing and Materials Processing* **2022**, *6* (4), 83. https://doi.org/10.3390/jmmp6040083.
(28) Hooper, P. A. Melt Pool Temperature and Cooling Rates in Laser Powder Bed Fusion. *Addit Manuf* **2018**, *22*, 548–559. https://doi.org/10.1016/j.addma.2018.05.032.
(29) Patel, S.; Vlasea, M. Melting Modes in Laser Powder Bed Fusion. *Materialia (Oxf)* **2020**, *9*, 100591. https://doi.org/10.1016/j.mtla.2020.100591.
(30) Jiang, H.; Yuan, G.; Cui, Z.; Zhao, Z.; Dong, Z.; Zhang, J.; Cong, Y.; Li, X. Effects of Support Types and Their Porosity Characteristics on the Catalytic Performance of Ni-Based Catalysts in Nitrobenzene Hydrogenation to Aniline. *Ind Eng Chem Res* **2023**, *62* (34), 13355–13367. https://doi.org/10.1021/acs.iecr.3c01327.
(31) Li, E. L.; Wang, L.; Yu, A. B.; Zhou, Z. Y. A Three-Phase Model for Simulation of Heat Transfer and Melt Pool Behaviour in Laser Powder Bed Fusion Process. *Powder Technol* **2021**, *381*, 298–312. https://doi.org/10.1016/j.powtec.2020.11.061.
(32) Wei, H. L.; Mukherjee, T.; Zhang, W.; Zuback, J. S.; Knapp, G. L.; De, A.; DebRoy, T. Mechanistic Models for Additive Manufacturing of Metallic Components. *Prog Mater Sci* **2021**, *116*, 100703. https://doi.org/10.1016/j.pmatsci.2020.100703.
(33) Benedetti, M.; du Plessis, A.; Ritchie, R. O.; Dallago, M.; Razavi, N.; Berto, F. Architected Cellular Materials: A Review on Their Mechanical Properties towards Fatigue-Tolerant Design and Fabrication. *Materials Science and Engineering: R: Reports* **2021**, *144*, 100606. https://doi.org/10.1016/j.mser.2021.100606.
(34) Masiagutova, E.; Cabanettes, F.; Sova, A.; Cici, M.; Bidron, G.; Bertrand, P. Side Surface Topography Generation during Laser Powder Bed Fusion of AlSi10Mg. *Addit Manuf* **2021**, *47*, 102230. https://doi.org/10.1016/j.addma.2021.102230.

(35) Yang, T.; Liu, T.; Liao, W.; MacDonald, E.; Wei, H.; Chen, X.; Jiang, L. The Influence of Process Parameters on Vertical Surface Roughness of the AlSi10Mg Parts Fabricated by Selective Laser Melting. *J Mater Process Technol* **2019**, *266*, 26–36. https://doi.org/10.1016/j.jmatprotec.2018.10.015.

(36) Kasperovich, G.; Becker, R.; Artzt, K.; Barriobero-Vila, P.; Requena, G.; Haubrich, J. The Effect of Build Direction and Geometric Optimization in Laser Powder Bed Fusion of Inconel 718 Structures with Internal Channels. *Mater Des* **2021**, *207*, 109858. https://doi.org/10.1016/j.matdes.2021.109858.

(37) Zhao, C.; Shi, B.; Chen, S.; Du, D.; Sun, T.; Simonds, B. J.; Fezzaa, K.; Rollett, A. D. Laser Melting Modes in Metal Powder Bed Fusion Additive Manufacturing. *Rev Mod Phys* **2022**, *94* (4), 045002. https://doi.org/10.1103/RevModPhys.94.045002.

(38) Farhang, B.; Ravichander, B. B.; Ma, J.; Amerinatanzi, A.; Shayesteh Moghaddam, N. The Evolution of Microstructure and Composition Homogeneity Induced by Borders in Laser Powder Bed Fused Inconel 718 Parts. *J Alloys Compd* **2022**, *898*, 162787. https://doi.org/10.1016/j.jallcom.2021.162787.

(39) Afrasiabi, M.; Keller, D.; Lüthi, C.; Bambach, M.; Wegener, K. Effect of Process Parameters on Melt Pool Geometry in Laser Powder Bed Fusion of Metals: A Numerical Investigation. *Procedia CIRP* **2022**, *113*, 378–384. https://doi.org/10.1016/j.procir.2022.09.187.

(40) Wang, R.; Garcia, D.; Kamath, R. R.; Dou, C.; Ma, X.; Shen, B.; Choo, H.; Fezzaa, K.; Yu, H. Z.; Kong, Z. In Situ Melt Pool Measurements for Laser Powder Bed Fusion Using Multi Sensing and Correlation Analysis. *Sci Rep* **2022**, *12* (1), 13716. https://doi.org/10.1038/s41598-022-18096-w.